JVSTA Journal of Vacuum Science & Technology A

Nanostructured thin films for hydrogen-permeation barrier

Motonori Tamura and Takashi Eguchi

Citation: Journal of Vacuum Science & Technology A **33**, 041503 (2015); doi: 10.1116/1.4919736
View online: http://dx.doi.org/10.1116/1.4919736
View Table of Contents: http://scitation.aip.org/content/avs/journal/jvsta/33/4?ver=pdfcov
Published by the AVS: Science & Technology of Materials, Interfaces, and Processing

Nanostructured thin films for hydrogen-permeation barrier

Motonori Tamura[a)]
Center for Industrial and Governmental Relations, The University of Electro-Communications, 1-5-1 Chofugaoka, Chofu, Tokyo 182-8585, Japan

Takashi Eguchi
Toho Kaken Co., Ltd., Koshigaya, Saitama 343-0822, Japan

(Received 12 January 2015; accepted 20 April 2015; published 6 May 2015)

The authors confirmed that applying a coating of Al_2O_3, TiC, or TiN on a substrate reduced the hydrogen permeation by a factor of at least one order of magnitude compared with uncoated substrates. Al_2O_3 films consisting of fine crystal grains, with diameters of about 40 nm or less, provided superior hydrogen-permeation barriers on the test specimens. The test specimens coated with TiN or TiC films, with columnar crystals grown vertically on the substrate, tended to exhibit higher hydrogen permeability. The microcrystalline structures with many grain boundaries are expected to provide effective hydrogen-barrier performance. © *2015 American Vacuum Society*.
[http://dx.doi.org/10.1116/1.4919736]

I. INTRODUCTION

The presence of hydrogen in many metallic materials, such as carbon steel,[1–5] stainless steel,[6–9] and aluminum alloys,[10–12] is widely known to negatively affect the mechanical characteristics. In particular, steel composed primarily of ferrite or martensite structures with higher strength is known to have high hydrogen diffusibility and strong tendency to suffer from hydrogen embrittlement.[1–3] There have been attempts in recent years to utilize hydrogen gas as an alternative to fossil fuel, leading to the development of numerous hydrogen-energy systems that use high-pressure hydrogen. Types 316 and 316L stainless steel are known to be suitable materials for structural components in hydrogen-energy systems and can endure embrittlement caused by a hydrogen environment.[13–16] For such industrial applications, it is important to understand the interactions between high-pressure hydrogen and materials and develop the appropriate technology to prevent hydrogen from permeating susceptible materials. Molecular hydrogen dissociates relatively easily to form hydrogen atoms on the surface of steel when exposed to a hydrogen gas atmosphere, and hydrogen permeation in steel has been reported to cause hydrogen embrittlement.[4,5]

Studies concerning hydrogen-barrier films have been conducted in a variety of fields such as nuclear fusion reactors, fuel cells, H_2S corrosion components, or vacuum equipment.[17–26] Dense ceramic films such as Al_2O_3, TiC, TiN, and BN have been reported to provide superior hydrogen-barrier performance. A diverse range of methods have been used to form these films, such as chemical vapor deposition, physical vapor deposition, or plasma-spray, and it is possible to reduce hydrogen permeation by creating a few folds in ceramic films with thickness of a few micrometers. The hydrogen-permeation reduction factors vary significantly from one report to another, however. The variance for Al_2O_3 is between 10 and 10 000, for example, owing to significant variations in hydrogen permeation behavior with the films' microstructures, which depend on the method of formation. Many engineers and researchers have experimented with the forming conditions to vary the microstructure of films and typical microstructures have been modeled.[27–30] For instance, in Thornton's structure zone model, microstructures are classified according to factors such as the substrate temperature and argon pressure during film formation.[27,28] There have been known a variety of microstructures such as columns of a few micrometers, coarse particle structures, or fine-grained structures of a few tens of nanometers by sputtering, but it would be difficult to believe that all these would result in identical hydrogen permeation behavior.

This study focused on the impact of differences in thin-film microstructures on hydrogen permeation behavior. The correlations between the two were investigated.

II. EXPERIMENT

A. Deposition process

Films were formed using the radio-frequency (RF) ion-plating method. Type 316L austenitic stainless steel was used for the substrates and various films were formed on one side of such substrates. Ultrasonically cleaned substrates were set inside the film-formation equipment, and the chamber was pumped to a vacuum before it was filled with argon. The surface of each substrate was then treated with ion bombardment under the argon atmosphere. The oxide film on the surface of the substrates was then removed, and a reactant gas was introduced to maintain the substrates at a constant temperature. Titanium or aluminum was melted by the evaporation source of the electron gun to generate a vapor of the metal, and the RF plasma of argon and the reactant gas were stabilized to form metal-based thin films.

We formed films of TiC, TiN, and Al_2O_3 under the conditions listed in Table I, which were selected for the formation of dense films with good adhesiveness while allowing for as much variation in grain sizes and microstructures within the films as possible by adjusting the output of the electron-gas power source, substrate voltage, RF output, reactant-gas pressure, substrate temperature, etc. Argon gas and reactant gases such as C_2H_2, N_2, and O_2 were introduced at a pressure

a)Electronic mail: mtamura@sangaku.uec.ac.jp

TABLE I. Coating conditions: P_{EB} = power of electron beam source, V_{DC} = substrate voltage, P_{RF} = power of RF. The operating pressure was 0.039–0.13 Pa. The substrate temperature was 413–573 K.

Coating	P_{EB} (kW)	$-V_{DC}$ (V)	P_{RF} (W)	Reactant gas
TiC	3.4–4.4	0.40–0.43	700	C_2H_2
TiN	2.7–3.8	0.40–0.43	700	N_2
Al_2O_3	1.3–3.8	0.15–0.27	400	O_2

of 0.039–0.13 Pa. The temperature of the substrates was maintained at 413–573 K. A film thickness of 2.0–2.5 μm was obtained for all films under these conditions.

B. Characterization of coatings

The crystalline phase of the films was analyzed using x-ray diffraction; the film thickness, film cross-sections, and microstructures were examined with a scanning electron microscope (SEM); the chemical composition of the films was analyzed by electron probe microanalyzer; scanning probe microscope (SPM) and cross-sectional transmission microscopy (XTEM) were employed to provide surface crystal grains and more detailed microstructural characterization.

The SPM is able to easily take measurements on test specimen surfaces in an ambient atmosphere and with high resolution. The analysis of film surface characteristics was carried out using various image-analysis software packages.[31–34] The images were processed by binarizing the irregularity on the surface of films to gain an understanding of the crystal grains in the films. The cross-sectional specimens of the films for XTEM were prepared using focus ion beam and analyzed for measuring grain size in the film. Average grain size in the film was obtained from five different area of observation.

C. Hydrogen-permeation tests

Hydrogen-permeation tests were performed on the coated stainless steel samples. These tests were based on the differential-pressure methods described in ISO15105-1:2007, the international standard for determination of gas-transmission rates.[35–37] This part of the standard specifies the use of a pressure sensor or a gas chromatograph for determining the gas-transmission rate of a single-layered plastic film or sheet and multilayered structures under a differential pressure. A gas chromatograph was used in this study.

Figure 1 shows a schematic illustration of the apparatus. The coated samples (diameter: 35 mm; thickness: 0.1 mm) were set on a silicon fiberglass susceptor, which was porous and could be held in place without bending at temperatures up to 773 K. The apparatus was evacuated to 10^{-6} Pa. After the test temperature stabilized, hydrogen (purity of 99.995%) was introduced into the susceptor side of the chamber at a filling pressure of 400 kPa. The stainless-steel-sample side of the apparatus was continuously evacuated. The samples were affixed with a metallic seal made of gold and could be heated by an electric furnace to 773 K without oxidation. The permeation area was 6.6 cm^2.

A thermal-conductivity detector (TCD) and a flame-ionization detector were used with the gas chromatograph.

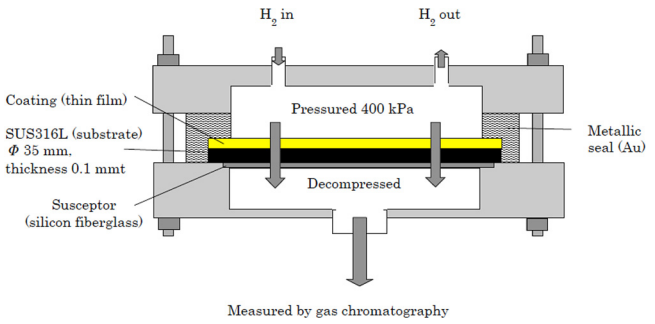

FIG. 1. (Color online) Schematic illustration of the experimental apparatus for hydrogen-permeation measurements.

The TCD consisted of four tungsten filaments in a temperature-controlled cell; this type of detector senses changes in the thermal conductivity of the column effluent and compares them to the flow of the carrier gas.

The permeability, Φ, is generally defined by the expression[25,35–37]

$$\Phi = J \cdot d/A \cdot \Delta p^n, \quad (1)$$

where J is the permeation flux of hydrogen through a sample of area A and thickness d, under a partial pressure gradient Δp across the sample called the driving pressure. The exponent n represents different permeation regimes: diffusion-limited and surface-limited when $n = 0.5$ and 1, respectively. Hydrogen permeation through a thin-film-coated steel sample is known to be diffusion-limited when the driving pressure is between 10^4 and 10^5.[25,35–38]

The permeation flux was continuously measured at a test temperature and under a test hydrogen pressure. After 30 min, for example, the standard deviation decreased below 10% among the data for permeation flux through the noncoated stainless steel substrate at 773 K under a hydrogen pressure of 400 kPa.

III. RESULTS AND DISCUSSION

A. Hydrogen-permeation mode

The permeation of hydrogen through solid materials proceeds via adsorption, dissociation, diffusion, and recombination coupled with desorption.[39–47] Figure 2 shows a schematic illustration of hydrogen permeation in coated samples. A hydrogen molecule ($H_{2,ad}$) is adsorbed on the surface of the film and decomposes to hydrogen atoms (H_{ad}). Such adsorbed hydrogen atoms diffuse into the film from the film surface ($H_{film,in}$) and move toward the interface with the substrate ($H_{film,out}$). Hydrogen atoms diffuse into the substrate from the interface of the film ($H_{sub,in}$) to the noncoated side of the substrate ($H_{sub,out}$). At the noncoated side of the substrate, the hydrogen atoms (H_{des}) form hydrogen molecules and desorption occurs. In this study, a driving force of hydrogen permeation was the pressure difference between the high- and low-pressure sides. Hydrogen permeation occurred in the film and the substrate because of decompression in the gas phase at the noncoated side of the substrate.

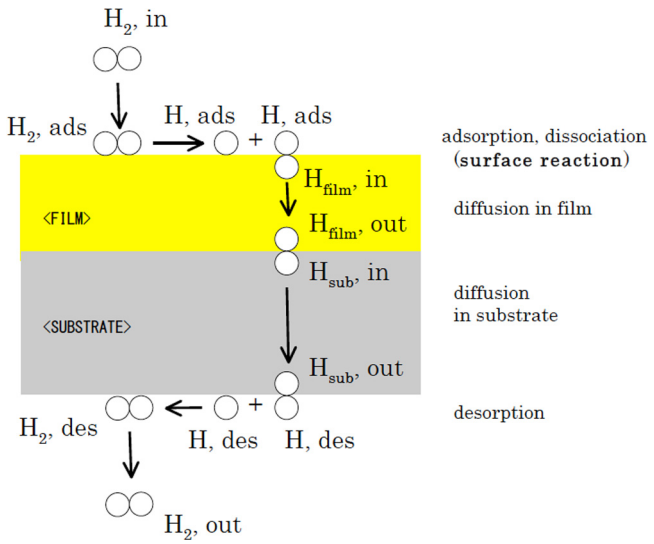

FIG. 2. (Color online) Schematic illustration of the permeation mechanisms.

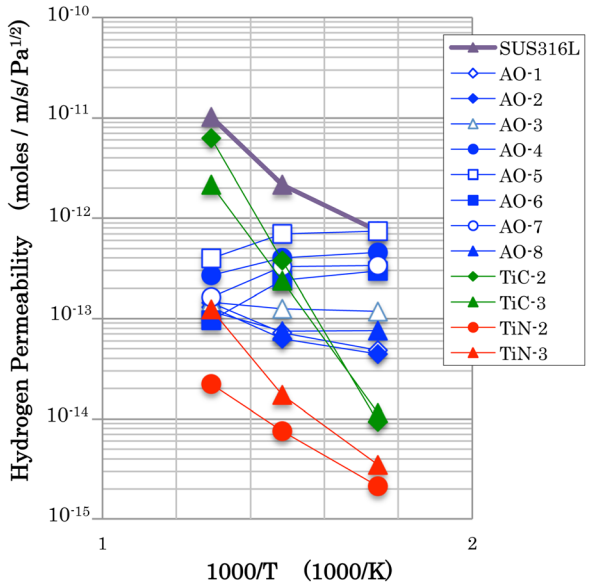

FIG. 3. (Color online) Arrhenius plot of hydrogen permeability as a function of temperature.

Our previous study[17] has demonstrated the dependence of permeation flux J on the driving pressure Δp in BN- and TiN-coated samples. The exponent n had a value of 0.48–0.53 at 573–773 K, which indicated that hydrogen passed through the samples in the diffusion-limited permeation mode. When $n = 0.5$ (diffusion-limited regime) in Eq. (1), the overall permeation flux of hydrogen through the sample can be given by Fick's law. In a steady state, the overall permeation flux J (measured in mol s^{-1}) through a sample of thickness $d_{\text{film}} + d_{\text{sub}}$ (d_{film}, thickness of film: 1.5×10^{-6} m; d_{sub}, thickness of substrate: 1.0×10^{-4} m) and area A (6.6×10^{-4} m^2) is expressed as

$$J = \Phi \cdot A((P_{\text{H2,in}})^{0.5} - (P_{\text{H2,out}})^{0.5})/(d_{\text{film}} + d_{\text{sub}}), \qquad (2)$$

where ϕ is the permeability of the sample as shown before, and $P_{\text{H2,in}}$ (4.0×10^5 Pa) and $P_{\text{H2,out}}$ (1.0×10^{-6} Pa) are the hydrogen pressures at the feed side and at the vacuum-pumping side, respectively.

B. Effect of microstructure of coatings on hydrogen-permeation behavior

The hydrogen-permeation behavior of specimens obtained in this study is shown in Fig. 3. Chemical compositions and crystal phases of some films are shown in Tables II–IV. The Al_2O_3, TiC, and TiN films were dense and had superior adhesion to the substrate. The hydrogen permeability decreased in all test specimens, which consisted of Al_2O_3, TiC, and TiN films on Type SUS316L substrates, confirming that the films performed effectively as hydrogen barriers.

The test specimens with a TiC or TiN coating underwent a significant change in hydrogen permeability, which depended on the test temperature, and the decline in the hydrogen permeability was greater at lower temperatures. Since the hydrogen permeability is a reflection of the diffusion of hydrogen in the film, the diffusion coefficient of hydrogen should also decrease with lower temperatures in TiC or TiN. In other words, the activation energy related to the dissipation of hydrogen is expected to be high.

On the other hand, the test temperature had little effect on the test specimens (AO-1, AO-2, AO-3, AO-4, AO-5, AO-6, AO-7, and AO-8), which were coated by Al_2O_3. Depending on the film, there was at least one order of magnitude difference in the value of hydrogen permeability. This difference in hydrogen permeability was examined in more detail with a particular focus on the role of the films' microstructure.

Table II shows the morphology and hydrogen permeability of Al_2O_3-coated test specimens.

A comparison of test specimens AO-8 and AO-5 revealed that they were both composed of microcrystalline grains equivalent to those in zone T (transition structure and densely packed fibrous grains) of Thornton's structure zone model.[27,28] There were differences in the crystalline grain sizes, however, with the hydrogen permeability being lower for the smaller grains of AO-8.

The relationship between the crystalline grain size and hydrogen permeability is shown in Fig. 4. Test specimens

TABLE II. Morphology and hydrogen permeability of typical Al_2O_3 thin films.

Sample No.	AO-8	AO-5
Film thickness (m)	2.03	2.35
Grain size (nm)	20.1	79.2
Surface roughness (nm)	1.57	6.06
Mole ratio: O to Al	1.48	1.47
Morphology of film	Zone T (fine grained)	Zone T (fine grained)
Hydrogen permeability (moles/m/s/$Pa^{1/2}$)		
573 K	7.59×10^{-14}	7.46×10^{-13}
673 K	7.49×10^{-14}	6.94×10^{-13}
773 K	1.18×10^{-13}	3.97×10^{-13}

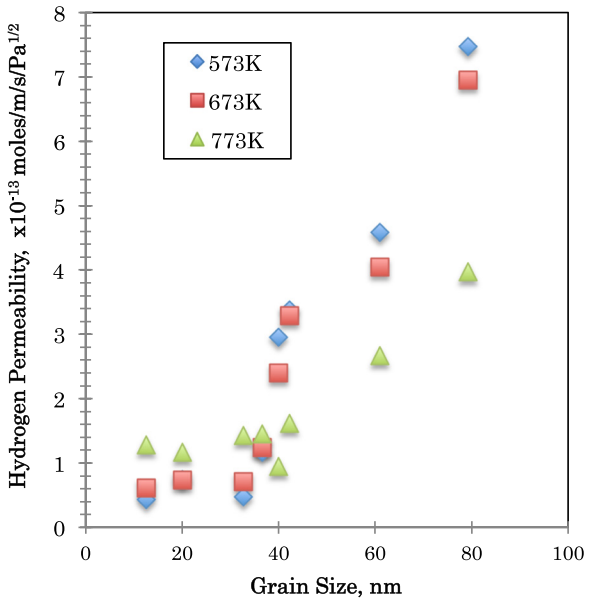

FIG. 4. (Color online) Hydrogen permeability of Al_2O_3-coated samples as a function of grain size in the films.

covered with films consisting of smaller crystalline grains tended to have lower hydrogen permeability.

Table III shows the morphology and hydrogen permeability of TiC-coated test specimens. The cross sections of the films and the morphology of the surface are shown in Figs. 5 and 6. A comparison of test specimens TiC-3 and TiC-2 revealed that TiC-3 was composed of microcrystalline grains equivalent to those in zone T of Thornton's structure zone model,[27,28] while the grains of TiC-2 were of a columnar shape similar to those in zone II (columnar) of the same model. There were also differences in the crystalline grain sizes, with higher hydrogen permeability for columnar TiC-2 grains with relatively larger size.

The same tendency was observed in test specimens covered with TiN. The morphology and the hydrogen permeability of TiN-coated test specimens are shown in Table IV. The cross sections of the film and the morphology of the surfaces are shown in Figs. 5 and 6. A comparison of test specimens TiC-2 and TiN-3 revealed that TiN-2 was composed of microcrystalline grains equivalent to those in zone T of Thornton's structure zone model,[27,28] while the columnar

TABLE III. Morphology and hydrogen permeability of typical TiC thin films.

Sample No.	TiC-3	TiC-2
Film thickness (μm)	2.50	2.50
Grain size (nm)	69	98
Surface roughness (nm)	1.56	1.56
Mole ratio: C to Ti	1.0	0.9
Crystal phase	TiC	TiC
Morphology of film	Zone T (fine grained)	Zone II (columnar)
Hydrogen permeability (moles/m/s/Pa$^{1/2}$)		
573 K	1.14×10^{-14}	9.29×10^{-15}
673 K	2.37×10^{-13}	3.78×10^{-13}
773 K	2.16×10^{-12}	6.27×10^{-12}

TiN-3 grains were equivalent to those in zone II (columnar). Similar to the case of TiC, there were also differences in the crystalline grain sizes, with higher hydrogen permeability for the columnar TiN-3 grains with relatively larger size. The TiC and TiN films with columnar structures tended to have relatively high hydrogen permeability.

Films consisting of microcrystalline grains equivalent to those in zone T of Thornton's structure zone model,[27,28] as shown in Fig. 5(a), were confirmed to have higher hydrogen-barrier performance. Many grain boundaries existed within the films, which could potentially present some form of obstruction when hydrogen passed through.

Studies concerning the state of hydrogen in materials[1–15,48–51] cited lattice defects (atomic vacancy, dislocation, and grain boundaries), impurity atoms, precipitates, inclusion boundaries, voids, etc., as hydrogen trap sites. Distinguishing the state of hydrogen has recently become possible with thermal desorption spectrometry and the like, based on the binding energy between such trap sites and hydrogen.

Studies on the hydrogen embrittlement mechanism of steel have been actively conducted since the 1970s. The critical mass and solid solubility of hydrogen that exists within a crystal lattice are derived from the amount of hydrogen in a pure iron test specimen in a highly pure hydrogen gas environment and equilibrium state.[1–4] The solid solubility is the atomic ratio of hydrogen with respect to the number of normal lattice, and the hydrogen concentration is known to be proportional to the square root of the hydrogen gas pressure.

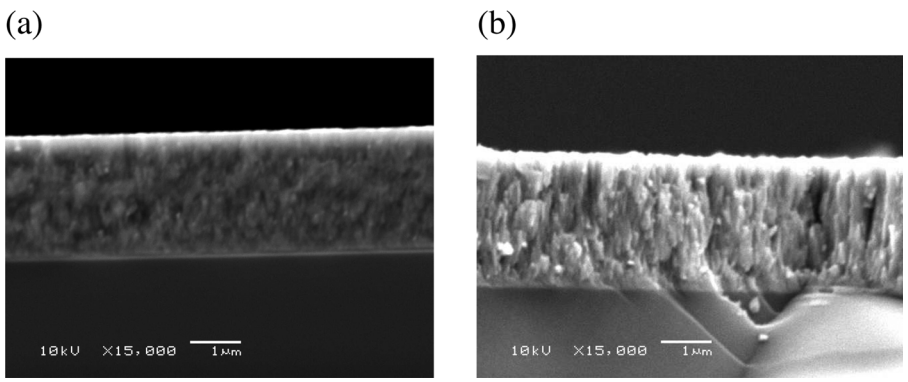

FIG. 5. SEM images showing morphologies of cross sections of (a) TiC-3 and (b) TiC-2. The sample numbers correspond to those in Table III.

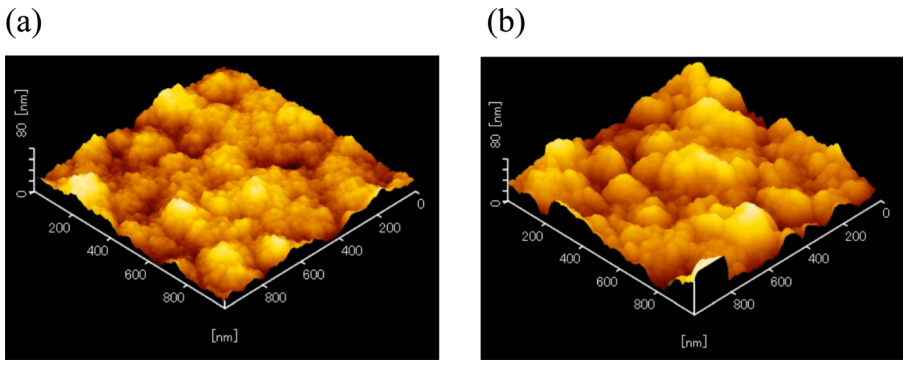

FIG. 6. (Color online) SPM images showing surface morphologies of (a) TiC-3 and (b) TiC-2. The sample numbers correspond to those in Table III.

The solid solubility of hydrogen in steel can be affected by the purity and surface condition of the test specimen, but the results of various researchers match quite well at about 673 K or higher.[1–5] The temperature dependence of solid solubility is close to a linear Arrhenius plot, which essentially suggests that there is a scenario associated with a solid solution, such as lattice interval positions occupied by hydrogen. Furthermore, the match between data in the literature and various test specimens signify that the amount of hydrogen that can be absorbed by iron is not much affected by impurities and other lattice defects, such as grain boundaries, at 673 K or higher temperatures.

In contrast, hydrogen solid solubility of a monocrystalline Ni test specimen is known to vary significantly from that of a polycrystalline test specimen of Ni.[50] At 573 K and lower temperatures, it has been pointed out that ferroalloys are also affected by surface absorption reactions and lattice defects.[5] The hydrogen diffusion coefficient in steel depends on the crystalline grain size and the diffusion coefficient decreases when the crystalline grain size is small.[51] The hydrogen content in Ni also depends on the crystalline grain size.[50] These findings led us to believe that the effects of grain boundaries cannot be ignored when the diffusion rate of hydrogen is relatively slow.

Hydrogen diffusion in steel has been known to be a few orders of magnitude lower in materials with ion covalent bonds, such as ceramic films,[18,19,26] and the hydrogen trap sites are believed to function sufficiently. Figure 7 shows schematically how grain boundaries become hydrogen traps. The microscale of a film's crystal grains is believed to have caused the grain boundaries to act as effective hydrogen-diffusion barriers.

TABLE IV. Morphology and hydrogen permeability of typical TiN thin films.

Sample No.	TiN-2	TiN-3
Film thickness (μm)	2.20	2.60
Grain size (nm)	56	92
Surface roughness (nm)	3.50	3.48
Mole ratio: N to Ti	0.9	0.9
Crystal phase	TiN	TiN
Morphology of film	Zone T (fine grained)	Zone II (columnar)
Hydrogen permeability (moles/m/s/Pa$^{1/2}$)		
573 K	2.12×10^{-15}	3.49×10^{-15}
673 K	7.58×10^{-15}	1.72×10^{-14}
773 K	2.21×10^{-14}	1.23×10^{-13}

IV. SUMMARY AND FUTURE DIRECTIONS

Films of Al_2O_3, TiC, and TiN produced by RF ion plating were dense and had superior adhesion to the substrate. The hydrogen permeability decreased by at least two orders of magnitude in all test specimens after the Type SUS316L substrates were coated with Al_2O_3, TiC, or TiN, confirming that the films exhibited hydrogen-barrier capabilities.

This difference in hydrogen permeability was examined with a focus on the microstructure of the films. Test specimens covered with Al_2O_3 films consisting of smaller crystalline grains, with diameters of about 40 nm or less, tended to have lower hydrogen permeability. These microcrystalline grains were equivalent to those in zone T of Thornton's structure zone model.

The TiC and TiN films with columnar structures and relatively large crystal grains equivalent to those in zone II (columnar) tended to have relatively high hydrogen permeability.

Many grain boundaries existed within the films of microcrystalline grains and we believe that such grain boundaries

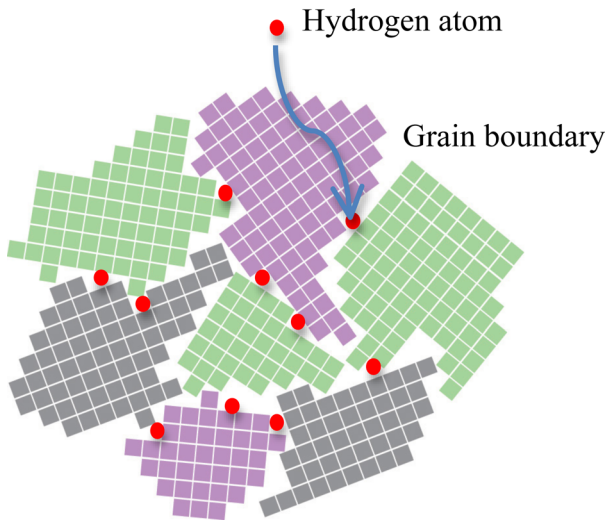

FIG. 7. (Color online) Hydrogen atoms can be trapped at grain boundaries in thin films.

could become hydrogen traps. The films of microcrystalline grains were confirmed to exhibit effective hydrogen-barrier functions.

Extensive studies of the correlation between film structure and deposition parameters have been carried out over the past ten decades. From an understanding of film formation, follows the possibility for micro- and nanostructural engineering in order to design a material for specific technological applications. This has led to the development and refinement of Thornton's structure zone models[27,28] that systematically categorize self-organized structural evolution during physical vapor deposition as a function of film growth parameters. The first structure zone models were derived from relatively low-resolution of optical and SEM observations. Later, cross-sectional TEM and SPM analyses were employed to provide more detailed structural characterization. *In situ* electron microscopy has revealed the dynamics of film growth. This, together with results from *in situ* SPM studies and computational materials science, has provided detailed atomistic insights into microstructural evolution during polycrystalline film growth.

In this study, behavior of hydrogen permeability of coated stainless steels was analyzed with a focus on the grain size of Al_2O_3 films. Thin films usually exhibit a wide variety of microstructures characterized in terms of not only grain size but also crystallographic orientation, lattice defects, phase composition, and surface morphology. Further study is necessary with a focus on the various microstructures to understand the correlation between the hydrogen permeation behavior and film microstructure and to develop high-performance hydrogen barrier coatings.

[1]A. R. Troiano, T. Am. Soc. Metal **52**, 54 (1960).
[2]C. D. Beachem, Metall. Trans. **3**, 437 (1972).
[3]J. P. Hirth, Metall. Trans. A **11**, 861 (1980).
[4]M. Nagumo, M. Nakamura, and K. Takai, Metall. Trans. A **32**, 339 (2001).
[5]K. Takai, Y. Homma, K. Izutsu, and M. Nagumo, J. Jpn. Inst. Met. **60**, 1155 (1996).
[6]M. B. Whiteman and A. R. Troiano, Corrosion **21**, 53 (1965).
[7]C. L. Briant, Metall. Trans. A **10**, 181 (1979).
[8]S. Fukuyama, K. Yokogawa, K. Kubo, and M. Araki, Trans. Jpn. Int. Met. **26**, 325 (1985).
[9]G. Han, J. He, S. Fukuyama, and K. Yokogawa, Acta Mater. **46**, 4559 (1998).
[10]S. Osaki, D. Itoh, and M. Nakai, J. Jpn. Inst. Light Met. **51**, 222 (2001).
[11]M. Ando, M. Senoo, and M. Kanno, J. Jpn. Inst. Light Met. **57**, 19 (2007).
[12]G. A. Young, Jr. and J. R. Scully, Metall. Trans. A **33**, 101 (2002).
[13]C. San Marchi, B. P. Somerday, and S. L. Robinson, Int. J. Hydrogen Energy **32**, 100 (2007).
[14]S. K. Lee, H. S. Kim, and S. J. Noh, J. Korean Phys. Soc. **5**, 3019 (2011).
[15]K. Horikawa, H. Okada, H. Kobayashi, and W. Urushihara, J. Jpn. Inst. Met. **74**, 199 (2010).
[16]M. Tamura and K. Shibata, J. Jpn. Inst. Met. **69**, 1039 (2005).
[17]M. Tamura, M. Noma, and M. Yamashita, Surf. Coat. Technol. **260**, 148 (2014).
[18]J. Yamabe, S. Matsuoka, and Y. Murakami, Int. J. Hydrogen Energy **38**, 10141 (2013).
[19]R. Checchetto, M. Bonelli, L. M. Gratton, A. Miotello, A. Sabbioni, L. Guzman, Y. Horino, and G. Benamati, Surf. Coat. Technol. **83**, 40 (1996).
[20]S. Sarkar, S. Datta, S. Das, and D. Basu, Surf. Coat. Technol. **204**, 391 (2009).
[21]C. Shan, A. Wu, Y. Li, Z. Zhao, Q. Chen, Q. Huang, and S. Shi, J. Nucl. Mater. **191–194**, 221 (1992).
[22]R. G. Song, Surf. Coat. Technol. **168**, 191 (2003).
[23]G. Zhang, S. Dou, Y. Lu, Y. Shi, X. Lai, and X. Wang, Int. J. Hydrogen Energy **39**, 610 (2014).
[24]N. Lee, S. Lee, K. Kim, W. Kim, H. Ju, D. M. Kim, and T. Hong, Int. J. Hydrogen Energy **38**, 7654 (2013).
[25]T. Chikada, A. Suzuki, Z. Yao, D. Levchuk, H. Mainer, T. Terai, and T. Muroga, Fusion Eng. Des. **84**, 590 (2009).
[26]G. W. Hollenberg, E. P. Simonen, G. Kalinin, and A. Terlain, Fusion Eng. Des. **28**, 190 (1995).
[27]J. A. Thornton, J. Vac. Sci. Technol. **11**, 666 (1974).
[28]J. A. Thornton, Annu. Rev. Mater. Sci. **7**, 239 (1977).
[29]J. W. Evans, P. A. Thiel, and M. C. Bartelt, Surf. Sci. Rep. **61**, 1 (2006).
[30]J. L. Plawsky, A. G. Fedorov, S. V. Garimella, H. B. Ma, S. C. Maroo, L. Chen, and Y. Nam, Nanoscale Microscale Thermophys. Eng. **18**, 251 (2014).
[31]D. A. Kiselev, I. K. Bdikin, E. K. Selezneva, K. Bormanis, A. Sternberg, and A. L. Kholkin, J. Phys. D: Appl. Phys. **40**, 7109 (2007).
[32]B. S. Lamsal, M. Dubey, V. Swaminathan, Y. Huh, D. Galipeau, Q. Qiao, and Q. H. Fan, J. Mater. **11**, 3965 (2014).
[33]P. Y. Huang *et al.*, Nature **469**, 389 (2011).
[34]S. Choi, J. Heo, D. Kim, and I. Chung, Thin Solid Films **464–465**, 277 (2004).
[35]S. A. Stern, J. Polym. Sci., Part A-2 **6**, 1933 (1968).
[36]JIS K7126-2:2006, Japanese Industrial Standards Committee.
[37]ISO15105-1:2007, International Organization for Standardization.
[38]E. Serra and A. Perujo, J. Nucl. Mater. **258**, 1028 (1998).
[39]M. P. Ariza, K. G. Wang, and M. Ortiz, Adv. Sci. Tech. **93**, 118 (2014).
[40]B. A. Szost, R. H. Vegter, and P. E. J. Rivera-Diaz-del-Castillo, Metall. Mater. Trans. A **44**, 4542 (2013).
[41]R. Hurlbert and J. O. Konecny, J. Chem. Eng. Phys. **34**, 655 (1961).
[42]A. Caravella, F. Scura, G. Barbieri, and E. Drioli, Chem. Eng. Sci. **63**, 2149 (2008).
[43]S. T. Oyama, M. Yamada, T. Sugawara, A. Takagaki, and R. Kikuchi, J. Jpn. Pet. Inst. **54**, 298 (2011).
[44]P. L. Andrew and A. A. Haasz, J. Appl. Phys. **72**, 2749 (1992).
[45]A. Pisarev, V. Shestakov, R. Hayakawa, Y. Hatano, and K. Watanabe, J. Nucl. Mater. **320**, 214 (2003).
[46]P. J. MacGuiness, M. Ceekada, V. Nemanic, B. Zajec, and A. Recnik, Surf. Coat. Technol. **205**, 2709 (2011).
[47]S. K. Lee, H. S. Kim, and S. J. Noh, J. Korean Phys. Soc. **59**, 3019 (2011).
[48]D. Gaude-Fugarolas, *Proceedings of Metal*, Brno. Czech Repubulic, EC (2013).
[49]R. Koyama and G. Itoh, Trans. Nonferrous Met. Soc. China **24**, 2102 (2014).
[50]A. Oudriss, J. Creus, J. Bouhattate, E. Conforto, C. Berziou, C. Savall, and X. Feaugas, Acta Mater. **60**, 6814 (2012).
[51]N. Yazdipour, D. Dunne, and E. Perelome, Mater. Sci. Forum **706–709**, 1568 (2012).